Supporting Information for

Unprecedented Zero Field Neodymium(III) Single-Ion Magnet Based on a Phosphonic Diamide

S. K. Gupta, T. Rajeshkumar, G. Rajaraman,* R. Murugavel*

Department of Chemistry, Indian Institute of Technology Bombay, Mumbai-400076, India

Experimental Section

Instruments and Methods. Infrared spectra were recorded on a Perkin Elmer Spectrum One spectrometer using KBr diluted pellets. Elemental analyses were performed on Thermoquest Flash EA 1112 series CHNS Elemental analyzer. The magnetic properties were measured using a Quantum Design MPMS-XL SQUID magnetometer equipped with a 7 T magnet in the temperature range 2-300 K using a polycrystalline powder samples. The data were corrected for the background diamagnetic contribution and the diamagnetic contribution of the compounds were corrected using Pascal's constants. Alternating current (ac) susceptibility measurements were performed with an oscillating ac field of 1 Oe oscillating at indicated frequencies between 0.1 and 1500 Hz. Magnetisation *vs* field plot at 1.8 K from + 4 T to - 4 T was recorded using Quantum Design SQUID-VSM.

Materials: Commercial grade solvents were purified by employing conventional procedures.[1] The phosphonic diamide ligand $^{t}BuPO(NH^{i}Pr)_2$ (**L**) was synthesized using a previously reported procedure.[2] $NdI_3.xH_2O$ were prepared from Nd_2O_3 (Alfa Aesar).

Synthesis of $[L_2Nd(H_2O)_5][I]_3\cdot L_2\cdot(H_2O)$. To a suspension of $NdI_3.xH_2O$ (0.20 mmol) in dichloromethane (20 mL) was added a solution of $^{t}BuPO(NH^{i}Pr)_2$ (0.264 mg, 1.2 mmol) in benzene (5 mL). The reaction mixture was stirred at 60 °C for 1 h and cooled down to room temperature. The solution was then filtered and the filtrate was kept for crystallization at ambient aerobic conditions. Block pale yellow crystals were obtained by the slow evaporation of the solvent. The product obtained was then thoroughly washed with toluene. Yield: 0.28 g (62 %, based on ligand). Anal. Calcd. for $C_{40}H_{112}I_3N_8Nd_1O_{10}P_4$: C, 31.73; H, 7.46; N, 7.40. Found: C, 32.03; H, 7.52; N, 7.16.

FT-IR (KBr, cm^{-1}): 3384 (s), 3271 (br), 2969 (vs), 2871 (s), 1619 (br), 1469 (s), 1419 (vs), 1386 (s), 1368 (s), 1311 (m), 1244 (w), 1146 (vs), 1130 (vs), 1112 (vs), 1092 (vs), 1049 (vs), 1022 (vs), 941 (w), 907 (m), 886 (m), 829 (m), 704 (m), 655 (s), 544 (m), 512 (w).

Single Crystal X-ray Crystallography

Suitable single crystals of **1** was selected and mounted on a Rigaku Saturn 724+ CCD diffractometer using paratone oil for unit cell determination and three dimensional intensity data collection. Data integration and indexing was carried out using CrystalClear and CrystalStructure.[3] The structures were solved using direct methods (SIR-97).[4] Structure refinement and geometrical calculations were carried out using programs in the WinGX module.[5] The final structure refinement was carried out using full least square methods on F^2 using SHELXL-2014.[6]

Table S1. Crystal data and structure refinement for **1**.

Identification code	CCDC 1451543
Empirical formula	$C_{40}H_{112}I_3N_8Nd_1O_{10}P_4$
Formula weight	1514.19
Temperature	120(2) K
Crystal system	Triclinic
Space group	*P* -1
a	13.7969(1) Å
b	14.7646(1) Å
c	20.728(2) Å
α	92.826(9)°
β	108.606(7)°
γ	114.956(8)°
Volume	3544.1(6) Å^3
Z	2
Absorption coefficient	2.175 mm^{-1}
Crystal size	0.18 x 0.14 x 0.09 mm^3
Reflections collected	27056
Independent reflections	12647 [R(int) = 0.0288]
Completeness to theta = 25.242°	98.50%
Data / restraints / parameters	12647 / 5 / 684
Goodness-of-fit on F2	1.056
Final R indices [I>2sigma(I)]	R1 = 0.0304, wR2 = 0.0751
R indices (all data)	R1 = 0.0311, wR2 = 0.0756
Largest diff. peak and hole	2.120 and -2.176 e.Å^{-3}

Table S2. Selected bond distances (Å) and angles (^{o}) in compound **1**.

Nd(1)-O(1)	2.285(2)	O(1)-Nd(1)-O(5)	85.73(8)	O(5)-Nd(1)-O(6)	70.32(8)
Nd(1)-O(2)	2.294(2)	O(1)-Nd(1)-O(6)	92.85(8)	O(5)-Nd(1)-O(7)	141.28(8)
Nd(1)-O(5)	2.436(2)	O(1)-Nd(1)-O(7)	92.58(8)	O(5)-Nd(1)-O(9)	73.99(8)
Nd(1)-O(6)	2.441(2)	O(1)-Nd(1)-O(8)	86.27(9)	O(6)-Nd(1)-O(7)	71.15(8)
Nd(1)-O(7)	2.443(2)	O(1)-Nd(1)-O(9)	89.34(8)	O(6)-Nd(1)-O(9)	143.95(8)
Nd(1)-O(8)	2.430(2)	O(2)-Nd(1)-O(5)	88.90(8)	O(7)-Nd(1)-O(9)	144.73(8)
Nd(1)-O(9)	2.457(2)	O(2)-Nd(1)-O(6)	86.72(8)	O(8)-Nd(1)-O(5)	145.34(8)
O(1)-Nd(1)-O(2)	174.43(8)	O(2)-Nd(1)-O(7)	92.54(8)	O(8)-Nd(1)-O(6)	143.80(8)
P(1)-O(1)-Nd(1)	155.49(14)	O(2)-Nd(1)-O(8)	97.35(9)	O(8)-Nd(1)-O(7)	72.74(8)
P(2)-O(2)-Nd(1)	149.49(14)	O(2)-Nd(1)-O(9)	87.75(8)	O(8)-Nd(1)-O(9)	72.25(8)

Table S3. SHAPE measures of seven co-ordinate relative to structures of **1**.[7]

Shape	Symmetry	Deviation
Johnson elongated triangular pyramid	C_{3v}	22.403
Johnson pentagonal bipyramid	D_{5h}	2.813
Capped trigonal prism	C_{2v}	5.587
Capped octahedron	C_{3v}	7.390
Pentagonal bipyramid	D_{5h}	0.286
Hexagonal pyramid	C_{6v}	24.491
Heptagon	D_{7h}	33.137

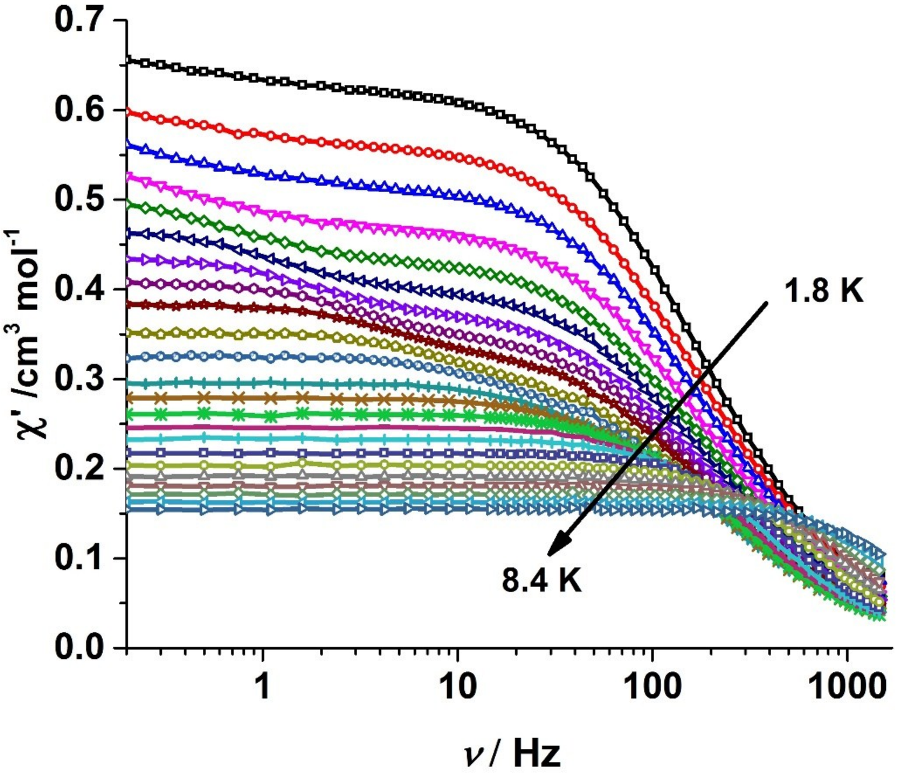

Figure S1. In-phase (χ_M') component of the ac susceptibility measured in an oscillating ac field of 1 Oe under zero dc field for complex **1**.

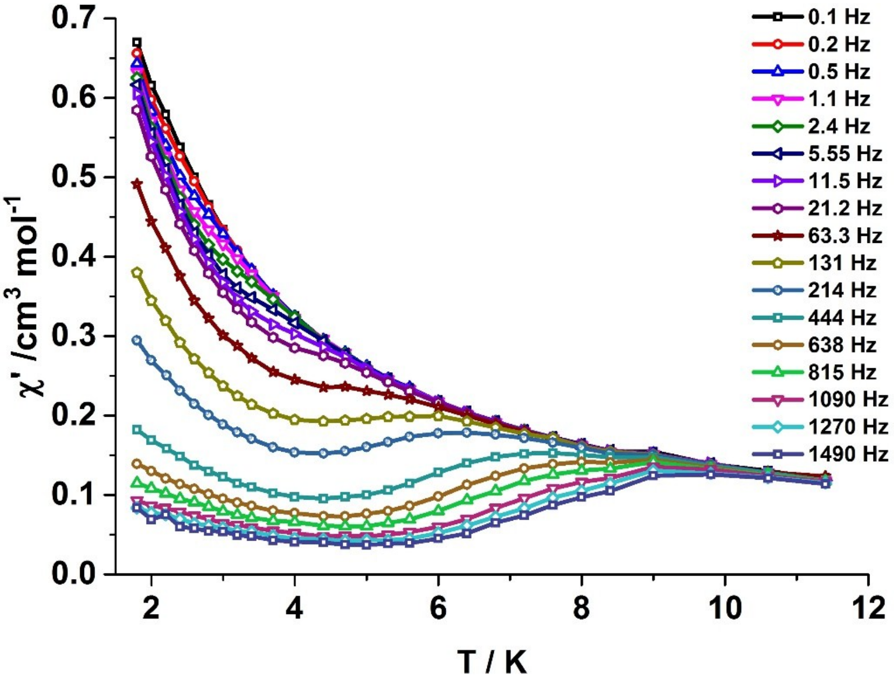

Figure S2. In-phase (χ_M') component of the ac susceptibility measured in an oscillating ac field of 1 Oe under zero dc field for complex **1**.

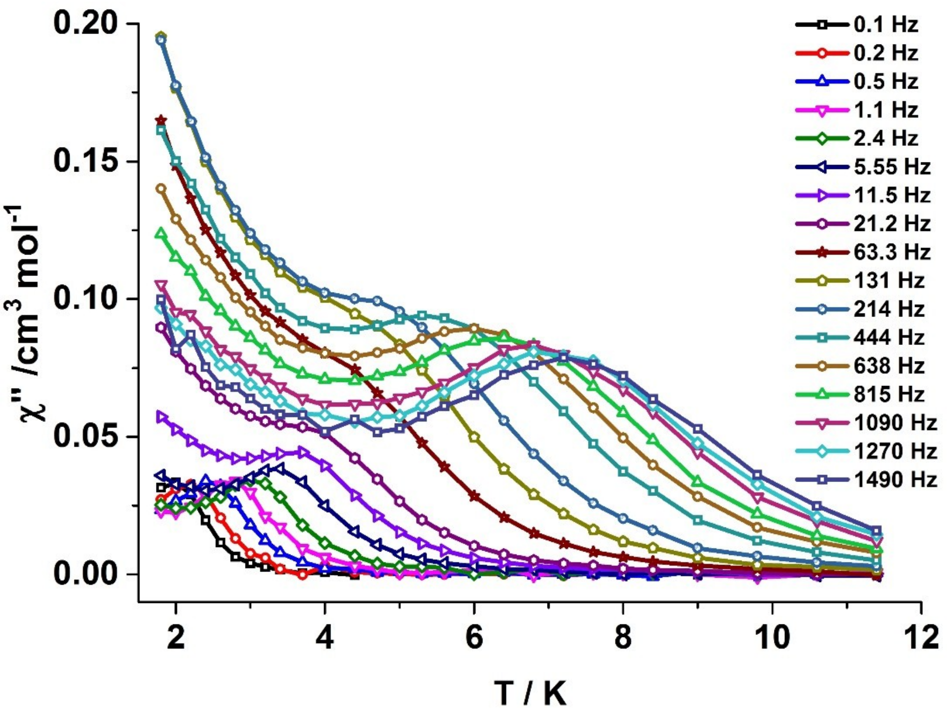

Figure S3. Out-of-phase (χ_M") component of the ac susceptibility measured in an oscillating ac field of 1 Oe under zero dc field for complex **1**.

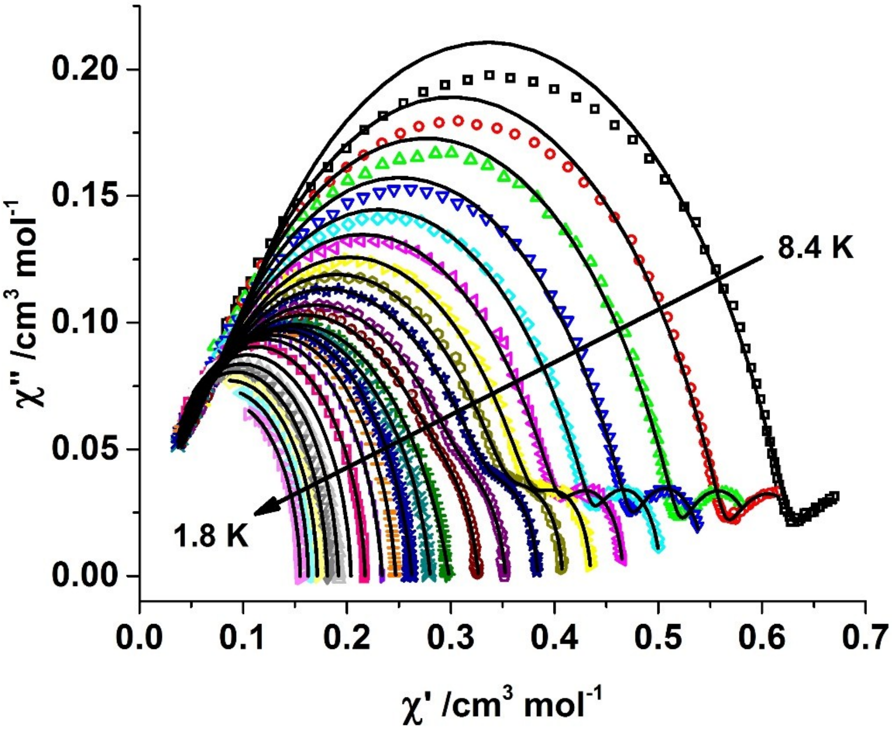

Figure S4. Plots of χ_M'' vs χ_M' under zero dc field. Solid lines are the fits with the Debye functions.

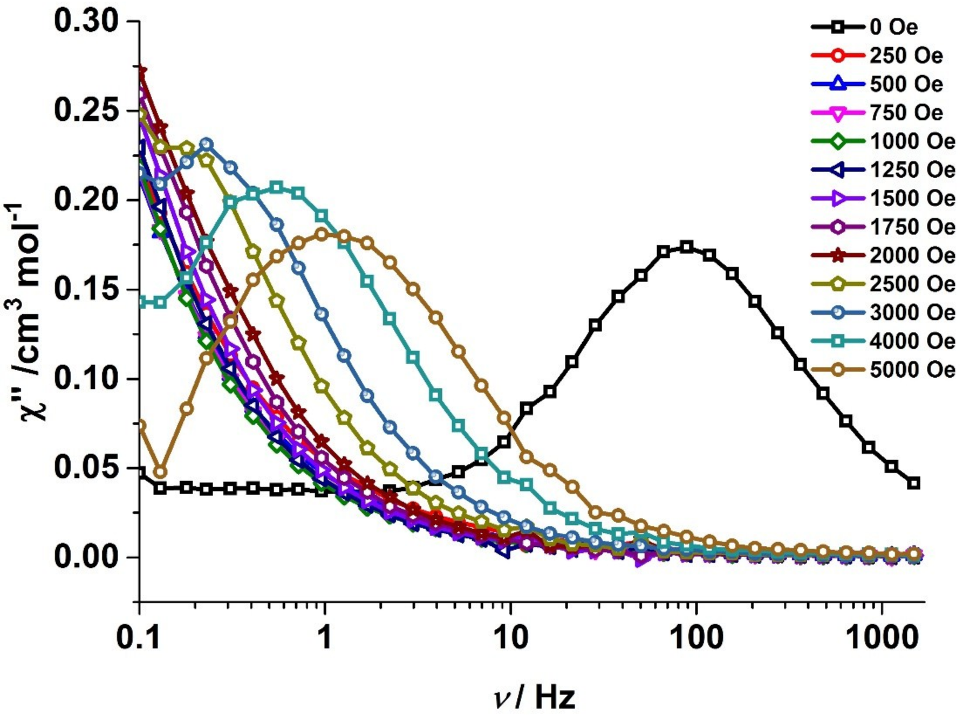

Figure S5. Frequency dependence of the out-of-phase (χ_M") component of the ac susceptibility measured in an oscillating ac field of 1 Oe under various applied dc fields at 1.8 K for complex **1**.

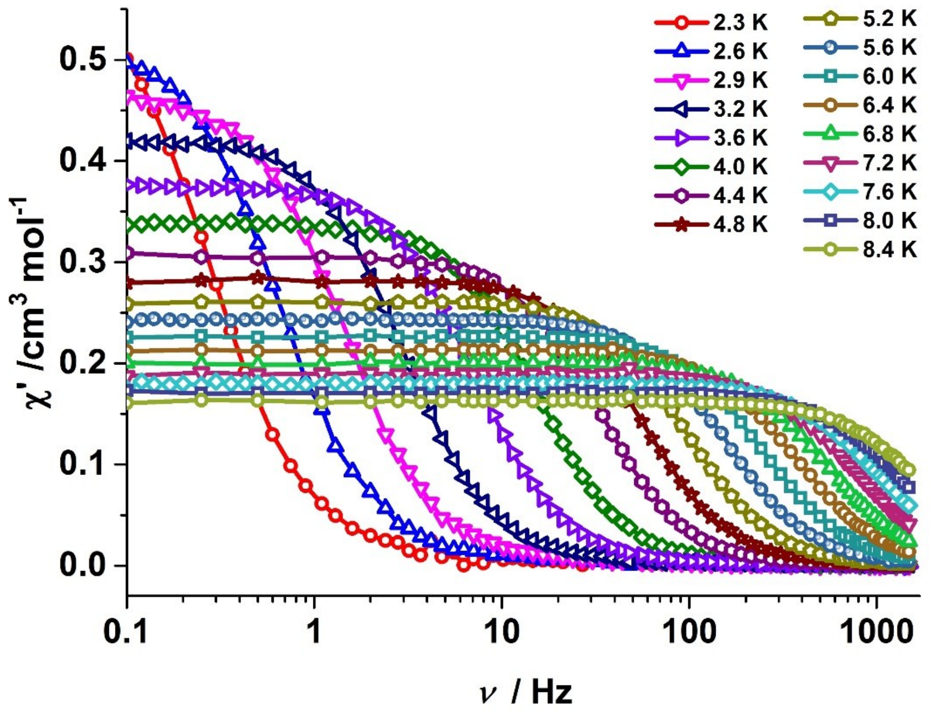

Figure S6. In-phase (χ_M') component of the ac susceptibility measured in an oscillating ac field of 1 Oe under an applied dc field of 2000 Oe for complex **1**.

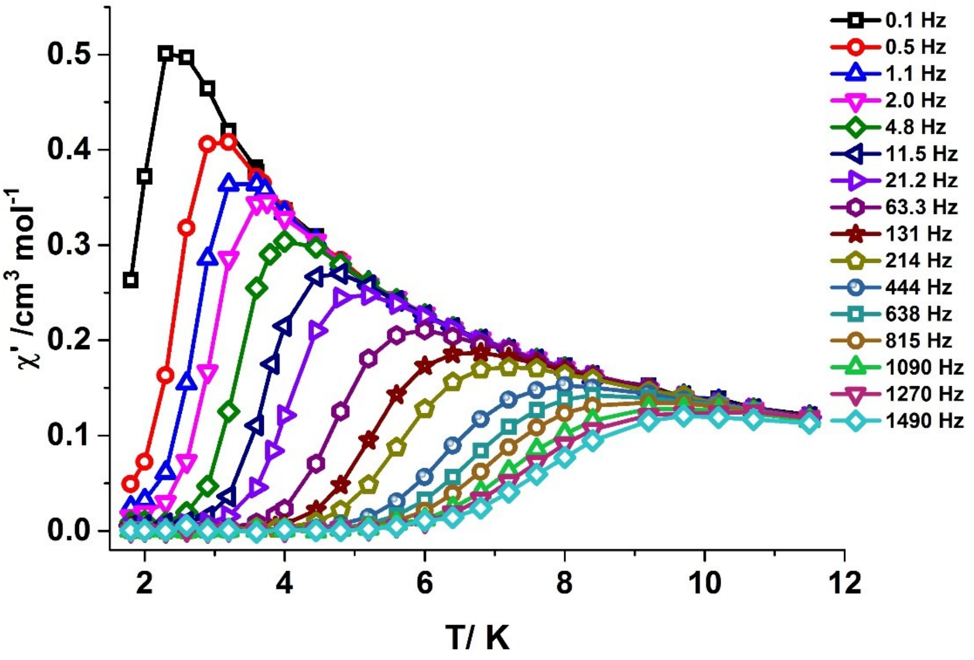

Figure S7. In-phase (χ_M') component of the ac susceptibility measured in an oscillating ac field of 1 Oe under an applied dc field of 2000 Oe for complex **1**.

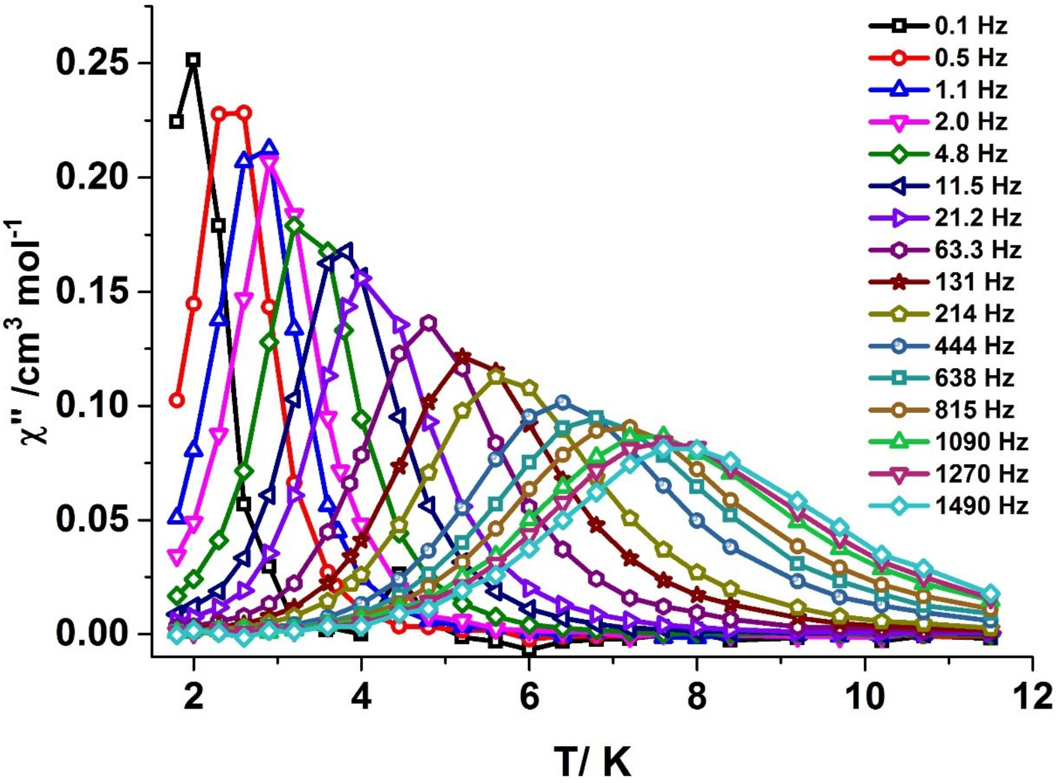

Figure S8. Out-of-phase (χ_M'') component of the ac susceptibility measured in an oscillating ac field of 1 Oe under an applied dc field of 2000 Oe for complex **1**.

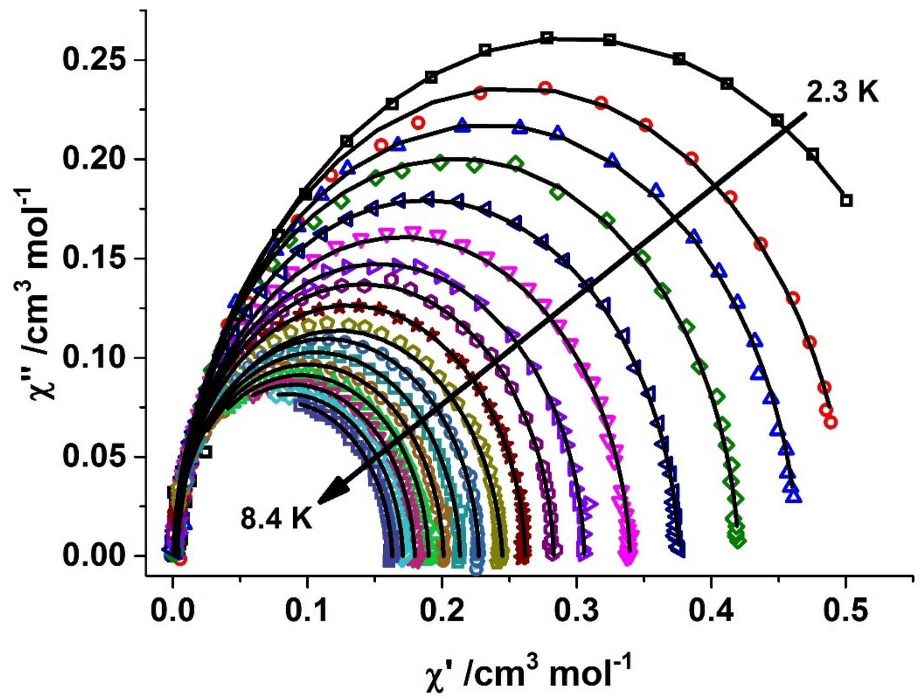

Figure S9. Plots of χ_M'' vs χ_M' under an applied dc field of 2000 Oe. Solid lines are the fits with the Debye functions.

Fitting of the relaxation time with multiple relaxation pathways for 1

Since fits to both the Arrhenius law (ln τ versus T^{-1}) and Cole-Cole (χ_M'' vs χ_M') plots for **1** indicate the presence of multiple relaxation process, the data for the relaxation process were treated with various relaxation pathways reported in the literature using the following equation (1),

$$1/\tau = 1/\tau_{QTM} + AH^2T + CT^n + \tau_o^{-1} \exp (U_{eff}/k_BT) \qquad ....(1)$$

where the first term corresponds to the relaxation process via quantum tunnelling pathway, the second term corresponds to the direct process, the third term models the relaxation via Raman process, and the fourth term accounts for the Orbach relaxation pathway.

Treatment of the slow relaxation process for **1** results in a reasonable fit with the QTM and Orbach pathway with negligible contribution from the Raman process (Figure S10). The values obtained from the best fit are $1/\tau_{QTM} = 971.51$ s^{-1} and n = 5, C = 4.21×10^{-18} s^{-1} K^{-5} (T). The application of dc field of 2000 Oe supresses the QTM pathway by lifting the degeneracy of the M_S levels. Best fit to the relaxation data with equation (1) indicates the Orbach and Raman relaxation pathways are dominant (Figure S11). The values obtained from the best fit are n = 5 and C = 0.0292 s^{-1} K^{-5} (T).

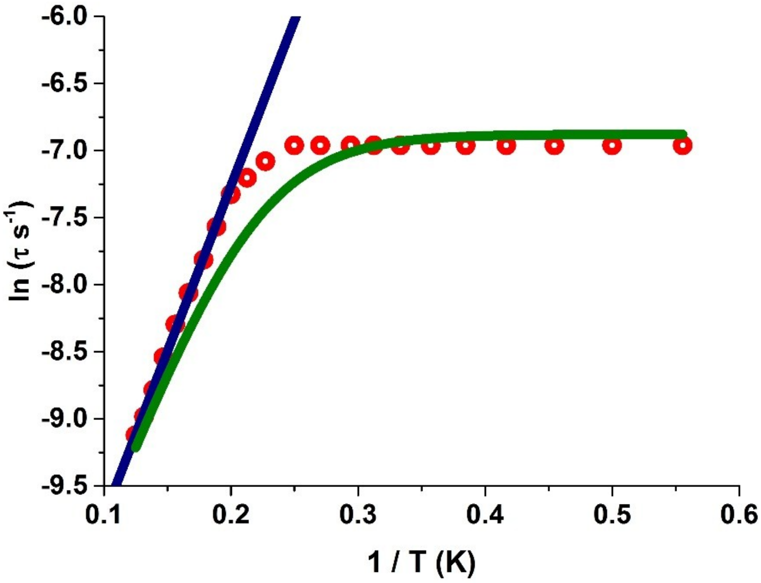

Figure S10. Plot of the relaxation time τ (T) (logarithmic scale) versus T^{-1} for **1** under zero dc field; the solid blue line represents fitting to the Orbach relaxation process and the green line represents the best fitting to the multiple relaxation pathways.

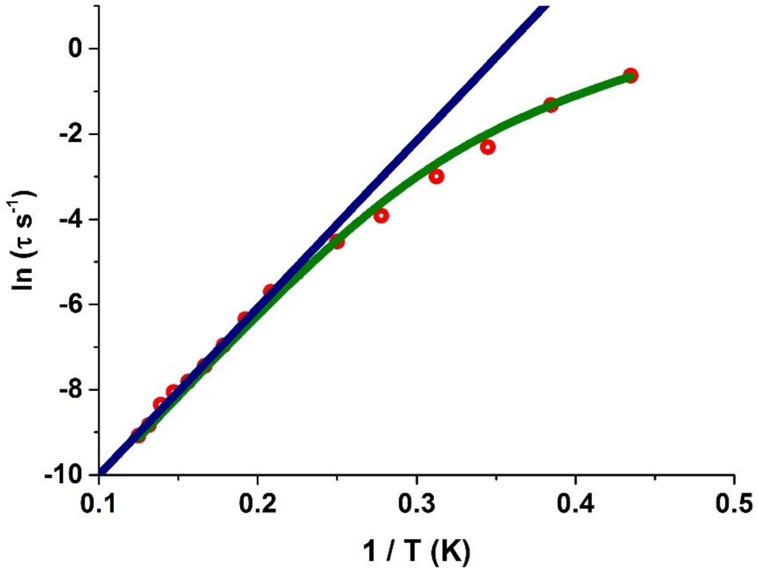

Figure S11. Plot of the relaxation time τ (T) (logarithmic scale) versus T^{-1} for **1** under an applied dc field of 2000 Oe; the dashed blue line represents fitting to the Orbach relaxation process and the solid green line represents the best fit to the multiple relaxation process.

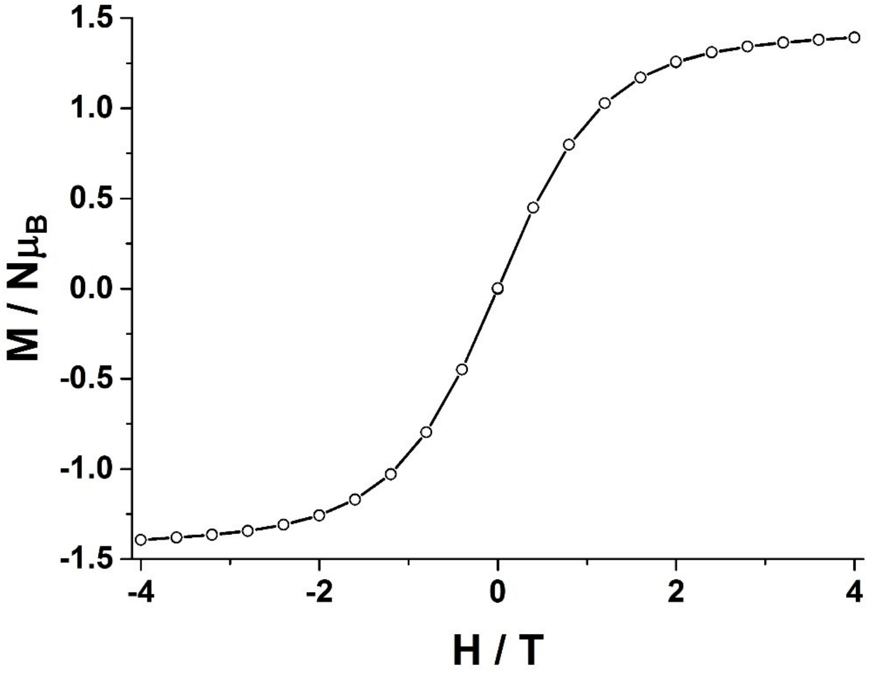

Figure S12. Magnetization vs field plot for **1** does not reveal any hysteresis effect. The field was swept from + 4 T to – 4 T and back at 1.8 K at an average rate of 0.015 T s^{-1}.

Computational Details

Ab initio calculations have been carried out on **1** to compute the *g*-tensors and the energies of the Kramers doublets. All the calculations have been performed using MOLCAS 7.8 quantum chemistry package. In this multi-configurational approach, relativistic approach has been treated based on Douglas-Kroll Hamiltonian. We have employed atomic natural (ANO-RCC) basis set for the calculations of *g*-tensor. The following contraction scheme has been employed [8s7p5d3f2g1h] for Nd, [3s2p] for N, [4s3p2d1f] for O, [6s5p2d] for I, [4s3p] for P, [3s2p] for C and [2s] for H. The ground state atomic multiplicity of Nd^{III} is $^4I_{9/2}$ which results in to five low-lying Kramers doublets. The CASSCF calculation comprises an active space of nine active electrons in the seven active orbitals (CAS (3,7)). With this active space, we have computed 35 quartets as well 112 doublet states in the CI procedure. After computing these excited states, we have mixed all these 35 quartets and 112 doublets using RASSI-SO module to compute the spin-orbit coupled states. In the last step we have used SINGLE_ANISO code[8] implemented in the MOLCAS to compute the *g*-tensors of Nd^{III}.

Table S4. SINGLE_ANISO computed energy barrier and angles between the g_{zz} axes of KDs for **1**

Energy (K)	g_{xx}	g_{yy}	g_{zz}	Angles between g_{zz} axis of KDs
0	0.02	0.02	6.29	-
302.2	0.10	0.42	5.10	69.39
400.0	0.48	1.25	4.88	85.77
441.13	0.32	0.87	4.87	78.69
599.13	0.95	0.96	4.88	3.09

Table S5. Composition of wave functions of the ground J = 9/2 of Nd(III) for complex **1** as derived from SINGLE_ANISO calculations.

w.f.	m_J	c_i		w.f	m_J	c_i	
		real	*imag.*			*real*	*imag.*
1	-4.5	-0.462108	-0.882303	2	-4.5	0.000000	0.000000
	-3.5	0.003383	0.012389		-3.5	0.000282	-0.001010
	-2.5	0.052776	-0.003744		-2.5	-0.002890	-0.006034
	-1.5	-0.035568	0.020296		-1.5	0.051277	0.018124
	-0.5	-0.001952	0.009228		-0.5	-0.001924	0.016119
	0.5	0.013386	-0.009183		0.5	-0.007269	0.006011
	1.5	-0.039846	-0.037015		1.5	0.001477	-0.040925
	2.5	-0.006685	0.000240		2.5	-0.021170	-0.048489
	3.5	0.000764	-0.000718		3.5	0.012544	-0.002751
	4.5	0.000000	0.000000		4.5	0.995993	0.000000
3	-4.5	-0.004141	0.038270	4	-4.5	0.004797	-0.044334
	-3.5	-0.034268	-0.046318		-3.5	0.044898	0.083129
	-2.5	-0.089610	-0.195125		-2.5	-0.255682	-0.253211
	-1.5	-0.042499	0.064297		-1.5	0.777921	0.023332
	-0.5	0.025786	-0.084270		-0.5	-0.357818	0.247477
	0.5	0.284536	-0.329117		0.5	0.086555	-0.016570
	1.5	0.060495	-0.775917		1.5	0.068496	-0.035335
	2.5	-0.224234	-0.281439		2.5	0.184352	0.110082
	3.5	-0.077816	-0.053581		3.5	-0.042362	-0.039052
	4.5	-0.044592	0.000000		4.5	-0.038494	0.000000

Table S6: CASSCF computed Mulliken charges

Atom Label	**1**
Nd1	1.2153
O1	-1.3319
O2	-1.3344
O5	-0.8722
O6	-0.9405
O7	-0.8402
O8	-0.8900
O9	-0.7869

References

1. W. L. F. Armarego, *Purification of laboratory chemicals / W.L.F. Armarego and D.D. Perrin*, Butterworth Heinemann, Oxford ; Boston, 1996.
2. R. Murugavel and R. Pothiraja, *New J. Chem.*, 2003, **27**, 968-974.
3. *CrystalClear (Version-SM Expert 2.0 r4, 2009) and CrystalStructure (Version 4.0, Rigaku, 2010), Rigaku Americas and Rigaku, The Woodlands, Texas, USA, and Rigaku Corporation, Tokyo, Japan.*
4. A. Altomare, M. C. Burla, M. Camalli, G. L. Cascarano, C. Giacovazzo, A. Guagliardi, A. G. G. Moliterni, G. Polidori and R. Spagna, *J. Appl. Crystallogr.*, 1999, **32**, 115-119.
5. L. Farrugia, *J. Appl. Crystallogr.*, 2012, **45**, 849-854.
6. G. Sheldrick, *Acta Cryst.*, 2015, **C71**, 3-8.
7. M. Llunell, D. Casanova, J. Cirera, J. Bofill, P. Alemany and S. Alvarez, *SHAPE (version 2.1)*, Barcelona, **2013**.
8. L. Chibotaru and L. Ungur, *The computer programs SINGLE_ANISO and POLY_ANISO*, University of Leuven, **2006**.